

Nanoscale

Accepted Manuscript



This is an *Accepted Manuscript*, which has been through the Royal Society of Chemistry peer review process and has been accepted for publication.

Accepted Manuscripts are published online shortly after acceptance, before technical editing, formatting and proof reading. Using this free service, authors can make their results available to the community, in citable form, before we publish the edited article. We will replace this *Accepted Manuscript* with the edited and formatted *Advance Article* as soon as it is available.

You can find more information about *Accepted Manuscripts* in the [Information for Authors](#).

Please note that technical editing may introduce minor changes to the text and/or graphics, which may alter content. The journal's standard [Terms & Conditions](#) and the [Ethical guidelines](#) still apply. In no event shall the Royal Society of Chemistry be held responsible for any errors or omissions in this *Accepted Manuscript* or any consequences arising from the use of any information it contains.

Precision Printing and Optical Modeling of Ultrathin SWCNT/C₆₀ Heterojunction Solar Cells

Sarah L. Guillot, Kevin S. Mistry, Azure D. Avery, Jonah Richard, Anne-Marie Dowgiallo, Paul F. Ndione, Jao van de Lagemaat, Matthew O. Reese, Jeffrey L. Blackburn

Abstract

Semiconducting single-walled carbon nanotubes (s-SWCNTs) are promising candidates as the active layer in photovoltaics (PV), particularly for niche applications where high infrared absorbance and/or semi-transparent solar cells are desirable. Most current fabrication strategies for SWCNT PV devices suffer from relatively high surface roughness and lack nanometer-scale deposition precision, both of which may hamper the reproducible production of ultrathin devices. Additionally, detailed optical models of SWCNT PV devices are lacking, due in part to a lack of well-defined optical constants for high-purity s-SWCNT thin films. Here, we present an optical model that accurately reconstructs the shape and magnitude of spectrally resolved external quantum efficiencies for ultrathin (7,5) s-SWCNT/C₆₀ solar cells that are deposited by ultrasonic spraying. The ultrasonic spraying technique enables thickness tuning of the s-SWCNT layer with nanometer-scale precision, and consistently produces devices with low s-SWCNT film average surface roughness (R_q of < 5 nm). Our optical model, based entirely on measured optical constants of each layer within the device stack, enables quantitative predictions of thickness-dependent relative photocurrent contributions of SWCNTs and C₆₀ and enables estimates of ~ 15 nm exciton diffusion lengths within each layer. These results establish routes towards rational performance improvements and scalable fabrication processes for ultra-thin SWCNT-based solar cells.

Introduction

Semiconducting single-walled carbon nanotubes (s-SWCNT) are promising candidates for the photo-absorbing material of inexpensive flexible photovoltaics because of their strong near-infrared (NIR) absorption and high carrier mobilities.^[1-4] The bandgaps of s-SWCNTs can be tuned by altering the nanotube diameter, allowing selective overlap with particular regions of the solar spectrum.^[5] For example, recent calculations for SWCNT solar cells containing four distinct SWCNT diameters predict a potential sunlight harvesting efficiency of 19 – 28%, with primary solar capture tuned either to the visible (28%, large band gap SWCNTs) or NIR (19%, small band gap SWCNTs).^[6] Such tunability may be beneficial for novel applications, such as building-integrated photovoltaic (BIPV) windows, where simultaneously high NIR absorbance and high visible transmittance are desirable. Importantly, the SWCNTs in PV devices are

typically coupled with other semiconductors (e.g. C_{60}) that establish a Type-II heterojunction, providing an energetic driving force for the exciton dissociation and charge separation that drives photocurrent.^[7-10] Current state-of-the-art *bilayer* SWCNT PV devices, based on s-SWCNT/ C_{60} bilayer heterojunctions, have reached AM1.5G power conversion efficiencies (PCE) of $\sim 1\%$,^[3] whereas *blended heterojunction* devices have recently attained PCE values of $\sim 2 - 3\%$.^[11, 12]

Although still slightly lower in efficiency relative to heterojunction devices, bilayer s-SWCNT/ C_{60} solar cells have exceptional diode qualities and internal quantum efficiencies, making them interesting model systems for ultrathin devices based on quantum-confined carbon active layers. The photocurrent extracted from such devices should depend sensitively on the exciton diffusion length within each layer (SWCNT and C_{60}), as well as the optical field distribution within the device, which depends sensitively on the precise thickness of each layer and can amplify the photocurrent extracted from specific regions of the solar spectrum.^[13] To probe such a model system, with optical properties defined by layers that can vary on the nanometer scale, it is important to develop methods for precision deposition of each corresponding layer, as well as models that can accurately account for the dependence of photocurrent generation on the optical field within the device. While fullerenes can be deposited with high precision by thermal evaporation, typical methods used previously for s-SWCNT deposition (e.g. doctor-blading,^[13] spin-coating^[14] or vacuum filtration^[15]) have several drawbacks, especially for printing uniform thin s-SWCNT films of prescribed thicknesses from organic solvent-based inks. Furthermore, detailed optical models of the SWCNT/ C_{60} device stack have thus far been hampered by a lack of measured optical constants for highly enriched s-SWCNTs.

In this study, we develop an ultrasonic spraying method for preparing bilayer heterojunction solar cells with monochiral (7,5) s-SWCNTs as the dominant source of NIR photocurrent generation. Atomic force microscopy (AFM) and optical profilometry measurements demonstrate that this spraying method produces smooth, uniform films with an average roughness of < 5 nm. This low surface roughness enables the fabrication of s-SWCNT/ C_{60} bilayer devices with significantly thinner C_{60} layers than other devices reported in the literature. Spectroscopic ellipsometry was used for the first time to determine the wavelength-dependent optical constants of (7,5) s-SWCNT thin films. We apply an optical model to calculate the optical field within our devices, using the measured thicknesses and optical constants of each layer as the only material property inputs. This model is able to accurately reconstruct the shape and magnitude of EQE spectra for devices with widely varying C_{60} layer thicknesses by assuming a ~ 15 nm exciton diffusion length (L_D) within both the C_{60} and s-SWCNT layers. The model also enables the prediction of particular device geometries that maximize photocurrent in different regions of the solar spectrum, an important advance for the future rational design of SWCNT/fullerene thin-film PV devices and photodetectors.

Experimental

Materials: Poly(9,9-dioctylfluorene-2,7-diyl) (PFO) was purchased from American Dye Source (Light Emitting Polymer ADS129BE). Toluene was purchased as ACS Reagent grade from Acros. SWCNT samples (SG65i-L43, -L48), synthesized from cobalt molybdenum catalysis of carbon monoxide disproportionation (CoMoCAT), were purchased from SouthWest NanoTechnologies. Poly(3,4-ethylenedioxythiophene)-poly(styrenesulfonate) (PEDOT:PSS) was purchased from Heraeus (Clevios™ P VP AI 4083). C₆₀ (Nano-C, >99.5%), bathocuprione (Aldrich, 96%), and silver pellets (Kurt J. Lesker, 99.99%, 1/8" x 1/8") were used for evaporation. Indium tin oxide substrates (ITO) were purchased from Thin Film Technologies and cleaned by scrubbing with diluted Liquinox detergent, followed by sonication in successive 10-minute acetone and isopropanol baths. The ITO substrates were then cleaned by 5 minutes of oxygen plasma in a Technics West 500-II model plasma etcher. All other materials were used as received.

Selective (7,5) SWCNT Dispersions and ink preparation: To isolate (7,5) SWCNTs, we ultrasonically dispersed CoMoCat SWCNTs in PFO and toluene.^[16] PFO (22 mg) was dissolved in 10 mL of toluene while heating (70 °C). SG65i (10 mg) was suspended in the PFO solution and sonicated for 30 minutes using a probe sonicator operating at 40% amplitude (Cole Palmer Model CPX 750, 20 kHz). The SG65i/PFO solution was centrifuged for 10 minutes at 13,200 rpm and 20 °C (Beckman-Coulter Optima L-100 XP Ultracentrifuge, SW32 Ti Rotor and Beckman-Coulter centrifuge tubes, polyallomer). A uniform SWCNT dispersion was obtained by decanting the supernatant by pipette, and filtering the supernatant through a kimwipe if precipitate particles were visible in the solution.

The SWCNT dispersion solution (40 mL) was then placed in a polyallomer centrifuge tube and centrifuged for 20 hours at 24100 rpm and 0 °C to remove excess PFO. The polymer/toluene supernatant was decanted and the SWCNT precipitate was sonicated in toluene using a water bath sonicator. Centrifugation was repeated with the same conditions until UV-vis-NIR analysis indicated that the mass ratio of PFO:SWCNT for the SWCNT ink sample was ~1:1.

Photovoltaic Device Fabrication: PEDOT:PSS was spin-coated in air at room temperature onto the cleaned ITO substrates (4000-4300 rpm, 60 seconds), followed by annealing in air at 120 °C for 10 minutes. The SWCNT ink was then spray-coated in air onto PEDOT:PSS/ITO substrates using ultrasonic spraying.^[17-19] The ultrasonic sprayer utilizes a Sonotek 120 kHz Impact nozzle. Room temperature SWCNT ink was sprayed at 400 µl/min under nitrogen flowing at 6.8 std L/min with 0.8 Watt ultrasonic spray head power. The substrate was heated to 130 ± 10 °C while spraying. UV-vis-NIR spectra and AFM profile measurements of these devices were used to estimate SWCNT layer thickness.

The sprayed ITO/PEDOT:PSS/(7,5) SWCNT films were soaked in toluene for 60 minutes at 70 °C to remove excess PFO. Thermal evaporation was used to deposit films of C₆₀ (1 Å/s) with varying thickness in the range of ~30 - 80 nm, followed by a 10 nm layer of bathocuproine (BCP) (0.5 Å/s) at 10^{-6} Torr in a glovebox-integrated evaporator (Angstrom Engineering NexDep Series) with a nitrogen atmosphere. The thickness of BCP was confirmed on a witness slide to be 10 nm \pm 20% by atomic force microscopy (Park ZE-70 system with Budget Sensors Tap300_G Tips). The thickness of the C₆₀ was calculated using the optical density of the peak at 422 nm (absorption coefficient, $1.21 \times 10^5 \text{ cm}^{-1}$).^[20] A 100 nm layer of the silver back contact was deposited by a separate, nitrogen atmosphere, glovebox-integrated thermal evaporation system (Angstrom Engineering EvoVac-600) at a rate of 0.8-1.8 Å/s. Samples were transferred between the gloveboxes using KF-sealed transfer tubes.

Spectrophotometry, Profilometry, Atomic Force Microscopy: Optical absorption data were collected with a Cary 500 Scan Spectrophotometer between 250 and 1400 nm using baseline correction. Optical profilometry was carried out on a Veeco Wyko NT1100 Optical Profiling System using phase-shifting interferometry. Atomic force microscopy (Asylum Research MFP-3D) images were generated in tapping mode using a <math>< 2</math> nm radius tip (NanosensorsTM SSS-NCHR).

Spectroscopic Ellipsometry Measurements: Optical constants of the SWCNT layers were determined using a variable angle spectroscopic ellipsometer (M-2000 VASE, J.A. Woollam Co). The measured ellipsometric parameters Psi (amplitude ratio) and Delta (phase difference) values were fitted by a Cauchy model to extract the refractive index $n(\lambda)$ and the extinction coefficient $k(\lambda)$, using the WVASE32® software package. The measurements were performed at 65°, 70°, and 75° angles of incidence, in the 190-1700 nm spectral range.

J-V and EQE Measurements: J-V measurements were taken in a glovebox on a solar simulator using a xenon arc lamp operating at 450 Watts (Newport Oriel Sol3A Class AAA Solar Simulator) under 1 sun, AM1.5 G illumination. The lamp was calibrated using a silicon reference diode (Hamamatsu S1336-8BQ). Light and dark J-V data were collected for a standard device of 0.101 cm² through a 0.061 cm² metal aperture from -1 V to 1 V. Data were not corrected for solar mismatch. The external quantum efficiency (EQE) was obtained using a frequency of 67 Hz, from a Newport Oriel system integrated into a nitrogen atmosphere glovebox using a Xenon light source. The system was calibrated with a Newport silicon and germanium combination detector.

Optical Modeling: Our optical model is based on the 2 x 2 scattering matrix formalism of Pettersson et al.,^[21, 22] and has been used successfully at NREL to calculate quantum efficiency in a number of different multi-layer PV devices, such as those based on quantum dot absorbers.^[23] The model calculates the optical electric field distribution within a device stack as a function of depth and wavelength, assuming isotropic and homogeneous layers separated by plane parallel interfaces. Material property inputs to the model include the index of refraction $n(\lambda)$, extinction

coefficient $k(\lambda)$ and thickness of each layer. Also included are the spectral irradiance, angle of incidence and polarization of the illumination, as well as reflections at the air/glass interface and dispersion within the glass substrate. From these inputs, the model calculates the spectral reflectance and transmittance of the device, the absorptance in each layer, and the wavelength-dependent generation rate $G(\lambda, x)$ (number of photons absorbed at each wavelength) depth in the device. At each wavelength, the average rate of photon absorption at a distance x into the device is proportional to the product of the modulus squared of the optical electric field $E(\lambda, x)$, the index of refraction $n(\lambda, x)$ and the absorption coefficient $\alpha(\lambda, x)$, divided by the photon energy $h\nu$:

$$G(\lambda, x) = \frac{c\epsilon_0\alpha(\lambda, x)n(\lambda, x)|E(\lambda, x)|^2}{2h\nu} \quad \text{Equation 1}$$

In equation 1, $\alpha(\lambda, x) = \frac{4\pi k(\lambda, x)}{\lambda}$.

Results and Discussion

Fabrication and Optical Characterization of SWCNT Films

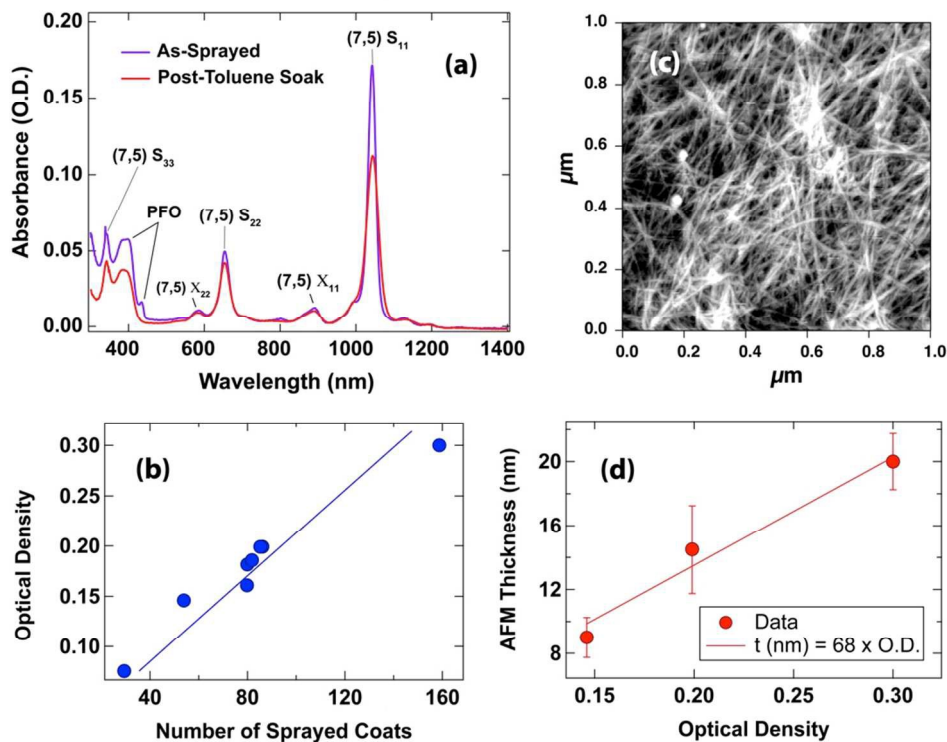


Figure 1. a) Soaking (7,5)-SWCNT spray-coated ITO films in toluene (70 °C, 60 minutes) resulted in peak broadening and height decrease for the S_{11} exciton transition. The peak area of the S_{11} transition was used to calculate comparative loss in film thickness due to toluene soaking. (b) SWCNT film absorbance can be adjusted with fine control by the number of coats sprayed at a given pump rate of solution. (c) AFM image (1 μm x 1 μm) of a SWCNT film, ~18 nm thick. (d) Film thickness can be approximated using the film absorbance, after correlating with AFM height measurements.

In this study, we employ nearly monochiral (7,5) s-SWCNT films as part of the photovoltaic active layer of bilayer SWCNT/C₆₀ thin-film solar cells. Metallic or small-bandgap s-SWCNTs can create traps and quench excitons and charges,^[10] thereby reducing photovoltaic efficiency for films with a high dispersity of different nanotube chiralities.^[24] SWCNT/C₆₀ bilayer heterojunctions with a SWCNT film containing five different chiralities have achieved a maximum external quantum efficiency (EQE) of 22% for excitation of the first SWCNT exciton transitions (S₁₁),^[25] while similar heterojunctions with a film of monochiral (7,5) SWCNTs achieved 34% EQE at S₁₁.^[13] Excess polymer removal is also important for fabricating efficient PV devices, as reducing the PFO:SWCNT ratio from 3.5 to 1.3 has been shown to increase EQE by ~150%, hypothesized to result from increased tube-tube coupling.^[25] For our devices, we removed excess PFO polymer to achieve a ~1:1 mass ratio of PFO:SWCNTs.

Following PFO removal, an ultrasonic spray system^[17-19] was used to deposit the (7,5) s-SWCNT active layer. Figure 1a displays the absorbance spectra of a thin (7,5) s-SWCNT film immediately after spraying onto a quartz slide (blue trace) and also after soaking the as-sprayed film in toluene at 70 °C (red trace). Several sharp peaks corresponding to the first and second excitonic transitions (S₁₁, S₂₂, S₃₃) and vibronic sidebands (X₁₁, X₂₂)^[26] of the (7,5) s-SWCNT are labeled. Only minor contributions from other s-SWCNTs are observed at ~1130 nm and 1190 nm ((7,6) and (8,6) s-SWCNTs, respectively), and analysis of the absorbance spectrum indicates these species represent less than 5% of the SWCNT population. Furthermore, no evidence can be seen for m-SWCNT impurities, as observed in our previous studies of polyfluorene-extracted s-SWCNTs.^[27] Several changes occur for the film absorbance following the toluene soak. The S₁₁ peak (1044 nm) broadens from 32 meV to 52 meV FWHM, indicating a change in dielectric environment and/or increased electronic coupling between SWCNTs. The primary broad absorbance peak of PFO (387 nm) decreases in intensity, indicating the removal of some PFO, and a small side peak observed at 430 nm disappears completely. This side peak has been attributed to extended backbone conjugation within the beta phase, and is a useful indication of PFO aggregation.^[28] The disappearance of this 430 nm shoulder indicates that the toluene soak removes a large proportion of PFO that presumably aggregates during solvent evaporation. Some of the SWCNTs are removed as well, as indicated by a reduction in the S₁₁ peak area, but to a much lesser extent than the PFO loss. After soaking, the integrated absorbance area of the PFO peaks is reduced by ~40%, whereas the SWCNT S₁₁ area is only reduced by ~5%.

The thickness of the s-SWCNT active layer can be controlled with good precision in the ultrasonic spray process simply by adjusting the number of sprayer passes for a given dispersion concentration and pump rate. Figure 1b demonstrates that the absorbance intensity of the S₁₁ peak increases linearly with the number of sprayer passes for films that have undergone the final toluene soak. This linearity demonstrates that the entire spray process is robust in generating uniform thin films with prescribed thicknesses. Such precision is difficult to achieve for techniques such as doctor blading, slot dye, and Gravure coating, especially for very thin films that are necessarily deposited from non-viscous dispersions.^[29] The morphological features of the

SWCNT films post-toluene soak were further characterized by atomic force microscopy (AFM), as shown in Figures 1c and 1d. The height profiles of several films, measured by AFM, were used to generate a calibration curve (Figure 1d) correlating the film thickness to the optical density of the S₁₁ peak (OD_{S11} , after the toluene soak) by UV-vis-NIR absorbance. Film thicknesses (t_{nm}) reported in this study were calculated by the linear fit of this calibration line ($t_{nm}=68 \times OD_{S11}$).

Topographical irregularities with heights on the scale of the acceptor (C₆₀) film thickness can lead to short-circuited devices or efficiency losses arising from low shunt resistance, so it is important to develop film deposition strategies that result in uniform films with low surface roughness over large areas. An important observation from the AFM measurements (Figure 1) is that the average surface roughness of the ultrasonic spray-deposited (7,5) s-SWCNT films was extremely low following the toluene soak. The surface roughness of the ~18 nm thick film shown in Figure 1c was ~2.5 nm, and the average surface roughness for the three films measured by AFM in Figure 1d was 3.8 ± 1.5 nm. To probe the film topography over larger areas, we turned to optical profilometry of films both before and after the toluene soak (Figure S1). Optical profilometry of the as-sprayed ~9 nm film (Figure S1a) demonstrates that the spray process leaves a residue of raised material (presumably PFO, SWCNTs, and potentially solvent impurities) in the form of circular droplets and some raised pillars. A recent study demonstrated that spraying from organic solvents (without surfactants) produced films with significant “coffee stain” rings formed by the rapidly drying droplets.^[30] These rings were removed by soaking the film in a warm solvent bath. Consistently, optical profilometry of the (7,5) s-SWCNT films post-toluene soak showed that the droplet residue features were smoothed out (Figure S1b). Analysis of the topography map for the *as-sprayed* film reveals an average surface roughness R_q (root mean squared) of 13-22 nm over a 300 μm x 230 μm surface. Following the 70 °C toluene soak, R_q was reduced by over 90% to 1.0-1.7 nm over a similar surface area.

Spectroscopic Ellipsometry and Device Modeling

To accurately predict the photocurrent for an ultrathin SWCNT/C₆₀ solar cell, it is necessary to understand the optical field distribution within the device. It is important to note that interference effects can lead to deviations of the EQE spectrum from the linear absorbance spectrum of the absorber layer. For example, Bindl et al. have demonstrated that adjusting the thickness of the C₆₀ layer enables tuning the spectral regions of constructive and destructive interference.^[13] However, optical constants for highly enriched s-SWCNT samples are lacking in the experimental literature, beyond a recent paper on (6,5) SWCNTs enriched by density gradient ultracentrifugation,^[31] making it difficult to accurately model the effects of changing the thickness of various layers on device photocurrent. To address this need, we characterized our (7,5) s-SWCNT thin films with spectroscopic ellipsometry to aid in the development of a full optical model of the bilayer PV device stack. Figures 2a and 2b display the wavelength-dependent raw ellipsometry parameters, Δ and Ψ , obtained at three different angles for a ~9 nm (as determined by absorbance/AFM) (7,5) s-SWCNT film. The spectra were successfully fit (red

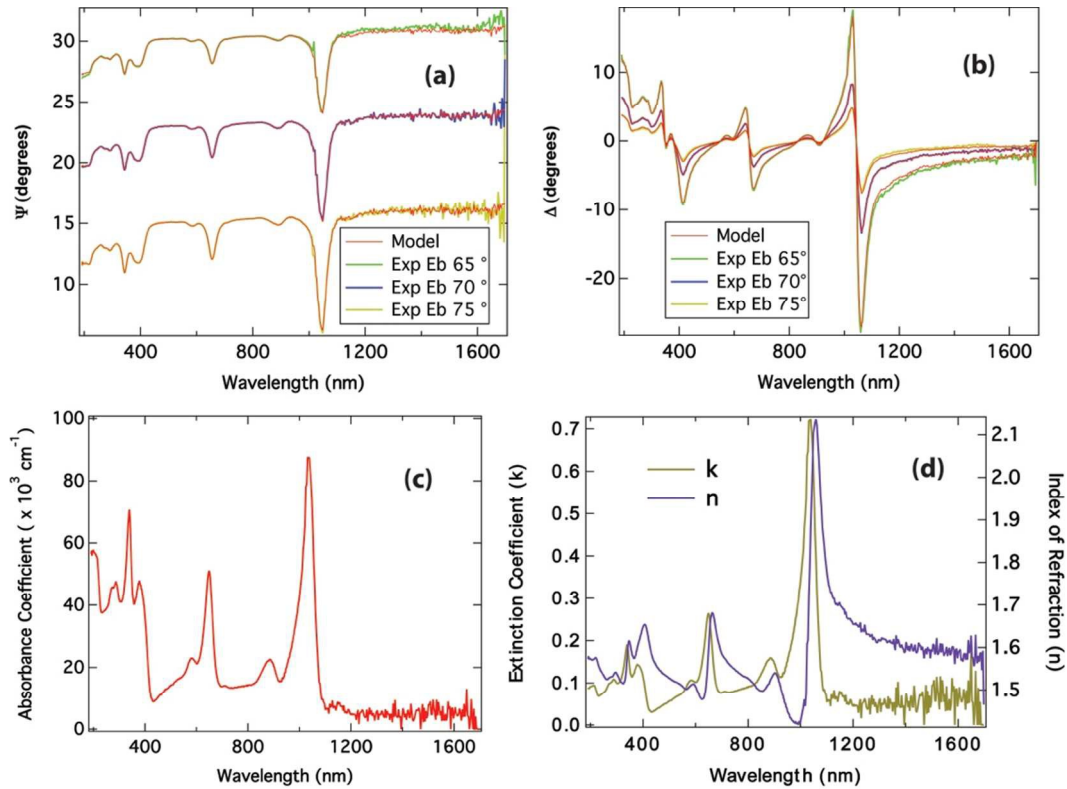


Figure 2. Spectroscopic Ellipsometry data for (a) psi (Ψ) and (b) delta (Δ) for three different incident angles. Red lines show the Cauchy model fit used to extract the (c) absorbance coefficient and (d) refractive index (n) and extinction coefficient (k)

traces) with a Cauchy model, with the best fits corresponding to a film thickness of 9.3 nm, consistent with the thickness obtained through the correlation of absorbance and AFM data (Fig. 1). Figure 2c displays the absorbance coefficient extracted from the modeled ellipsometry data, and 2d displays the extracted refractive index (n) and extinction coefficient (k). We note one important caveat for the optical constants displayed in Figure 2. In contrast to SWCNTs enriched by e.g. DGU, our PFO-enriched (7,5) s-SWCNT films have $\sim 1\%$ by weight PFO remaining bound to the SWCNTs in the film. The absorbance from this residual PFO produces features in the wavelength-dependent optical constants in the range of $\sim 350 - 400$ nm that are not related to the (7,5) s-SWCNTs.

To model the thickness-dependent interference effects on EQE spectra, we utilize an optical model of the device stack that is parameterized with the complex index of refraction for each layer as calculated from spectroscopic ellipsometry data.^[23] Ellipsometry data for each layer were obtained experimentally at NREL and modeled with the multiphase model, as described above for the (7,5) s-SWCNT layer.^[23] Figure 3a shows a two-dimensional map of the predicted photocurrent as a function of SWCNT and C_{60} thickness for the device stack shown in the figure inset. The map in Figure 3a was generated by assuming that each component of the absorber layer (SWCNT and C_{60}) may be characterized by an exciton diffusion length, L_D . Our model

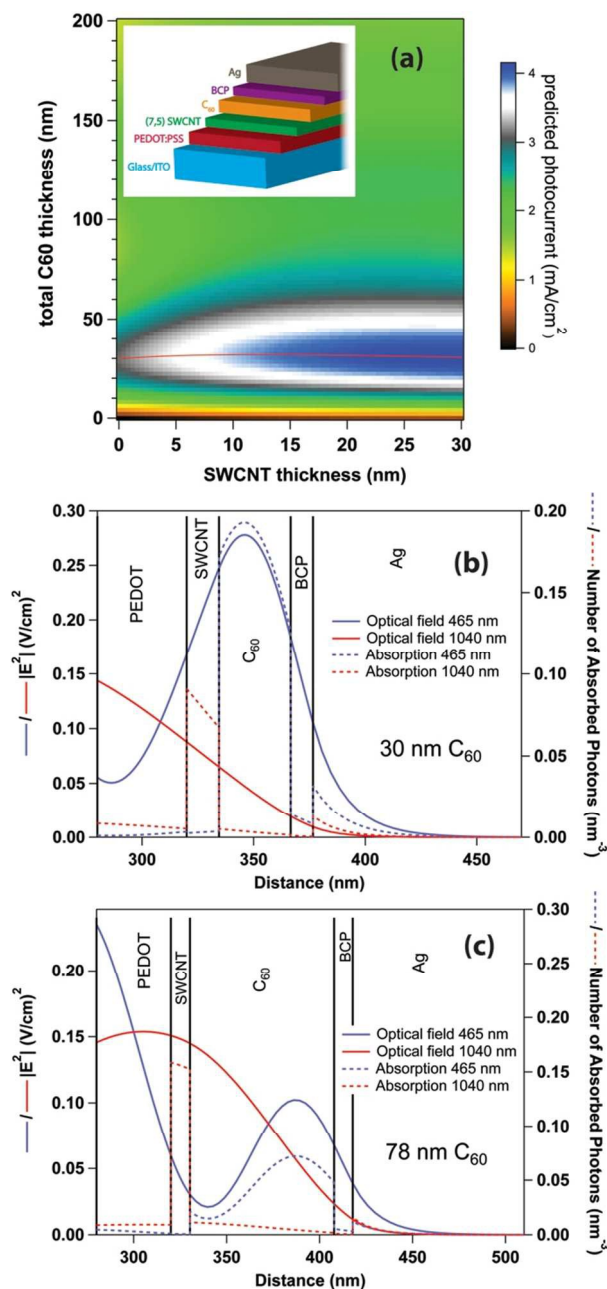


Figure 3. (a) Two-dimensional map of predicted J_{sc} for devices with varying SWCNT and C₆₀ layer thickness. Red line traces the maximum J_{sc} . The model for panel (a) assumes a SWCNT L_D of 10 nm and C₆₀ L_D of 15 nm. Inset of panel (a) shows a schematic of the device stack used in this study. (b) and (c) display the distribution of optical field (solid lines) and absorption (dashed lines) for 1040 nm (red) and 465 nm (blue), as calculated by the optical model for (b) device with 10 nm (7,5) SWCNT layer and 30 nm C₆₀ layer, and (c) devices with 10 nm (7,5) SWCNT layer and 78 nm C₆₀ layer. In (b) and (c), the penetration distance into the cell begins at the ITO/PEDOT interface (280 nm).

assumes that the percentage of photogenerated excitons reaching the interface to produce photocurrent ($X_{J_{sc}}$) decays exponentially with distance (d) from the interface as: $X_{J_{sc}} \propto e^{-(d/L_D)}$

The map in Figure 3a is generated with a SWCNT L_D of 10 nm and a C₆₀ L_D of 15 nm, in congruence with recent estimates of the singlet exciton diffusion length within C₆₀ and s-SWCNT films, as well as the experimental J_{sc} values of our own devices (*vide infra*). In particular, device and optical studies have estimated C₆₀ L_D values of ~ 7 nm,^[32-34] ~ 10 nm,^[35] and ~ 19 nm^[36] within similarly evaporated thin films. Preliminary studies of multi-chiral s-SWCNT/C₆₀ PV devices suggest L_D values in the range of ~ 8 nm as the mass ratio of wrapping polymer to s-SWCNTs approaches 1.3:1,^[25] whereas this value may increase for the monochiral devices with $\sim 1:1$ PFO:SWCNT ratio studied here.

An obvious outcome from the model is that the photocurrent is optimized for the device geometry utilized in our study at a relatively thin C₆₀ layer, that ranges from ~ 29 nm to 32 nm (red trace in Fig. 3a), depending on the SWCNT thickness. The precise C₆₀ thickness at which photocurrent is optimized will depend sensitively upon the electron and hole transport layers utilized in the device, and can vary for different device architectures. However, for the device architecture used here, which is a standard architecture for organic photovoltaics, Figure 3a emphasizes the importance of producing extremely smooth SWCNT layers, as achieved through the ultrasonic spray process, so that thin acceptor layers can be utilized to optimize device performance without encountering significant failure rates (short

circuiting) or fill factor losses (shunting).

It is important to note that the general shape of the map does not change significantly when modifying the C_{60} and s-SWCNT L_D values. Whereas the *magnitude* of all J_{SC} values within the map does increase by increasing the L_D values, the *optimum C_{60} thickness* is determined primarily by the wavelength-dependent optical field distribution within the device that results from constructive and destructive interference upon reflection from the silver cathode. To clarify this point, Figures 3b and 3c display the calculated optical field and absorption as a function of optical penetration distance into two separate devices. Whereas both devices contain 10 nm (7,5) SWCNT films, the C_{60} thickness is either 30 nm (Fig. 3b) or 78 nm (Fig. 3c). The wavelengths displayed are representative of either the peak of the (7,5) S_{11} (1040 nm, red traces) or the visible peak of C_{60} absorption (465 nm, blue traces). For the device with 30 nm of C_{60} , the peak of the 465 nm optical field is located within the C_{60} layer, ~ 11 nm away from the SWCNT/ C_{60} interface. Importantly, this places the optical field at a position closely matched to the range expected for the C_{60} singlet exciton diffusion length.^[32-36] The peak of the 1040 nm optical field is outside of the absorber layer, instead being maximized within the ITO layer (below 280 nm, not shown). Thus, this cell geometry should optimize absorption in the visible portion of the spectrum within the C_{60} layer. In contrast, for the device with 78 nm of C_{60} , a local maximum of the 465 nm optical field is still located within the C_{60} layer, but it is ~ 60 nm away from the SWCNT/ C_{60} interface, well outside the expected C_{60} singlet L_D . The 1040 nm optical field, however, is near its maximum within the (7,5) SWCNT layer. Thus, this cell geometry should optimize absorption in the near-infrared portion of the spectrum within the SWCNT layer. Consequently, the photocurrent produced by each device depends on the integral of the resulting external quantum efficiency (EQE) spectrum with the AM1.5 solar spectrum.

(7,5) SWCNT/ C_{60} Solar Cells by Ultrasonic Spraying

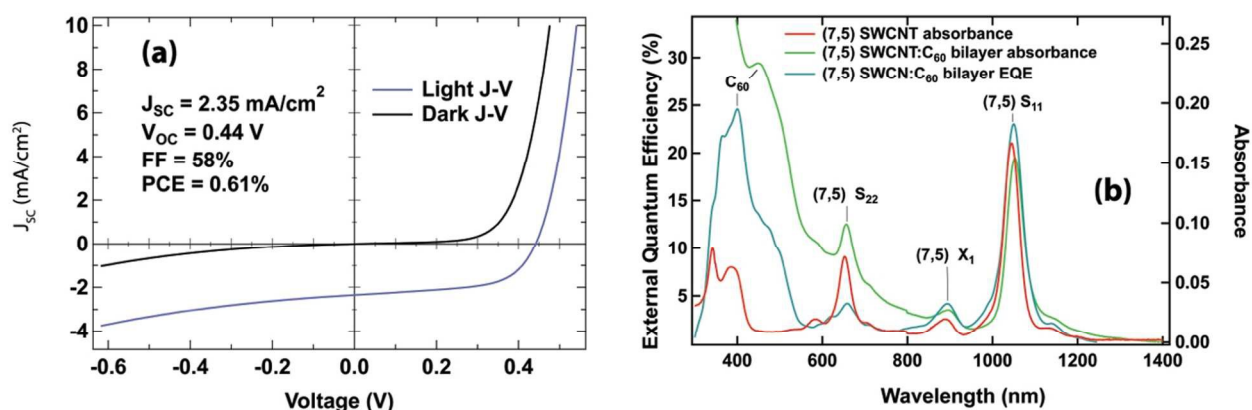


Figure 4. (a) Light (blue trace) and dark (black trace) J-V curves of a bilayer device with ~ 10 nm (7,5) SWCNT layer and ~ 78 nm C_{60} layer, under 1 sun AM1.5G irradiance (blue line). (b) EQE spectrum of the device in panel (a), overlaid with the absorbance spectra of the neat SWCNT and bilayer films.

To test the utility of the ultrasonic spraying method and the accuracy of our optical model, we prepared a series of bilayer SWCNT PV devices with $\sim 10 - 14$ nm (7,5) thin films

sprayed by ultrasonic spraying. Figure 4a shows dark and light J-V curves for a device prepared with a ~10 nm thick (7,5) s-SWCNT layer and a ~78 nm thick C₆₀ layer. The device demonstrated a short-circuit current (J_{SC}) of 2.35 mA/cm², an open-circuit voltage (V_{OC}) of 0.44 V, a fill factor (FF) of 58%, and a power conversion efficiency (η_{PCE}) of 0.61%. At approximately -0.2 V, the device displays an onset of reverse bias leakage current. While the open circuit voltages of the sprayed devices evinced variation between sprayed devices, overall these devices achieved a maximum V_{OC} of 0.46 V, significantly greater than the max V_{OC} previously reported for similar doctor-bladed devices (0.38 V).^[3] In contrast to previous SWCNT PV devices,^[3, 8, 13] we find that a hole transport layer (PEDOT:PSS for this study) is necessary to rectify the current flow in our spray-coated devices. We hypothesize that this hole transport layer may contribute to the higher V_{OC} , but further measurements are necessary to confirm this hypothesis. The J-V characteristics were also measured with a 610 nm long pass (LP) filter to quantify the SWCNT contribution. The S₁₁ and S₂₂ transitions of (7,5) carbon nanotubes occur at 1044 nm and 653 nm respectively, while C₆₀ absorbs around 330 nm, with a prominent shoulder at ~465 nm. With the 610 LP filter in place, the J_{SC} was reduced to 44% of the unfiltered current density, indicating that the SWCNTs provide a substantial portion of the photocurrent in our devices.

The EQE spectrum of this device (Figure 4b) matches the salient features of the absorbance spectrum very well over the entire visible and NIR range. In particular, the spectral shapes, energies, and linewidths of the (7,5) excitonic and vibronic peaks are conserved in the EQE spectrum. As seen by a comparison of the absorbance spectrum of the film to its EQE spectrum in Figure 3c, the NIR EQE maximum of 23% occurs precisely at the S₁₁ transition (1044 nm). Using the AM1.5G solar irradiance spectrum and the EQE shown in Figure 3c, the expected J_{SC} was calculated. The EQE-predicted J_{sc} (2.64 mA/cm²) is within 13% of the J_{sc} measured at AM1.5G (2.35 mA/cm², Figure 3). Figure S2 compares the EQE-calculated J_{SC} and the J_{SC} measured by the solar simulator for a number of different devices. The EQE values are all within 16% of the measured J_{SC} but more often overestimate than underestimate the current. The slight overestimation of the EQE-calculated J_{SC} for most devices likely arises from the fact that the EQE spectra measured here are not DC light-biased, and are thus measured at significantly lower photon fluxes than used in the AM1.5 solar simulator. Figure S3 demonstrates a slight sub-linear dependence on J_{sc} with photon flux, which would contribute to an overestimation of integrated J_{sc} from EQE spectra.

Correlation of Predicted and Experimental J_{SC} and EQE

The relative weighting of absorption features in the EQE spectrum (Fig. 4b) is tied directly to the optical field distribution within this device (Fig. 3c). For example, although a small peak in the EQE is seen at the S₂₂ transition wavelength (653 nm), the ratio of EQE for S₁₁ and S₂₂ excitation is heavily biased towards the S₁₁ due to a maximum in the optical field in the SWCNT layer for 1040 nm (Fig. 3c) and a minimum for 650 nm (not shown in Fig. 3c). Since the wavelength-dependent optical field is a sensitive function of the thickness of each layer, we

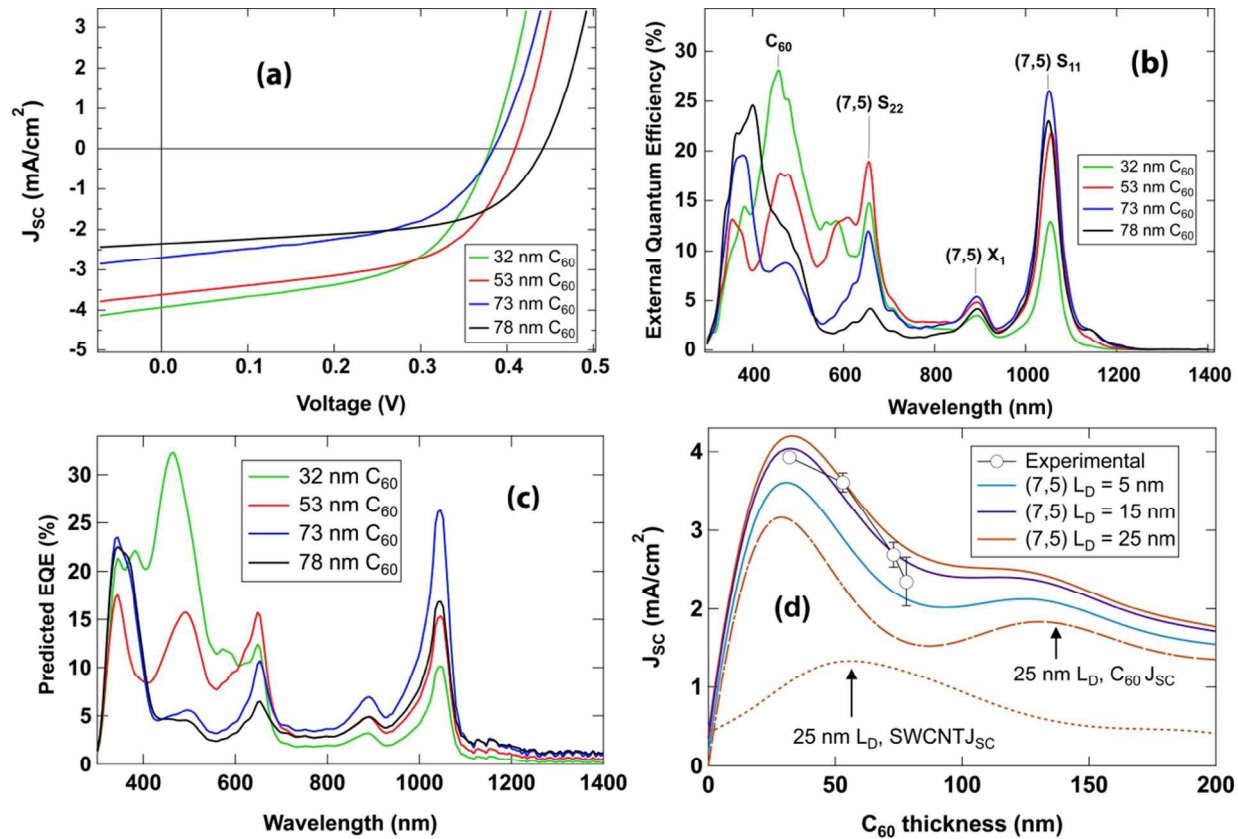


Figure 5. Differences in performance between devices with various thicknesses of C_{60} . (a) J-V curves of devices with different thicknesses of C_{60} . (b) Experimental EQE spectra for the same devices shown in (a). (c) Modeled EQE spectra for the devices shown in (a). (d) Comparison of experimental J_{sc} values (open circles) to predicted J_{sc} (solid lines) for a 13 nm SWCNT layer in contact with a C_{60} layer with $L_D = 15$ nm. The model is run with three different SWCNT L_D values – 5 nm (blue), 15 nm (violet), 25 nm (orange). For the 25 nm SWCNT L_D case, the SWCNT and C_{60} contributions to J_{sc} are broken out as the dashed and dash-dotted lines, respectively.

explored interference effects further by systematically varying the C_{60} layer thickness. Figures 5a and 5b display J-V curves and EQE spectra, respectively, for devices prepared with 10 - 14 nm s-SWCNT thickness and with C_{60} thicknesses of approximately 30, 50, 70, and 80 nm. As shown in Figure 5a and tabulated in Table 1, the device with ~ 30 nm C_{60} displayed the maximum current density (3.93 mA/cm^2) of all our devices, with a fill factor of 54%. The current density, averaged over many devices for each C_{60} thickness, increased with decreasing C_{60} layer thickness, reaching a maximum at 32 nm C_{60} thickness, in agreement with the behavior predicted by Figure 3a.

The dependence of J_{sc} on C_{60} thickness results from systematic variations of the EQE spectra of these devices (Figure 5b), which modify the contributions of the SWCNT and C_{60} layers, as summarized in Table 2. Consequently, the photocurrent produced by each device depends on the integral of the resulting external quantum efficiency (EQE) spectrum with the AM1.5 solar spectrum. Figure 5c shows the EQE spectra predicted by our optical model for each of the solar cells shown in Figures 5a and 5b. Similar to the photocurrent map in Figure 3a, the spectra in Figure 5c were generated by assuming a characteristic exciton diffusion length, L_D , within both the (7,5) SWCNT and C_{60} layers. The best fits to the experimental EQE data were

obtained with an L_D value of ~ 15 nm for excitons in the C_{60} layer and L_D values in the range of $\sim 5 - 25$ nm for excitons in the SWCNT layer. The fits in Figure 5c are all generated with $L_D = 15$ nm for the SWCNT layer. The most significant deviations between the predicted and measured EQE spectra occur in the range of 300 – 500 nm. These deviations likely arise from (1) artificial contributions of PFO spectral features to the (7,5) optical constants, discussed above, and (2) errors in the optical constants of ITO in this region, where reflections from the ITO produce interference fringes. Modeling of the patterned ITO layer used in our devices produces some unavoidable error, due to the experimental spot size for the ellipsometry measurement slightly exceeding the size of the patterned ITO pads. Despite slight deviations, the model accurately reconstructs the overall shapes of the EQE spectra in both the visible and NIR, accounting for the observed contributions of the s-SWCNT layer and C_{60} layer to the photocurrent as a function of C_{60} thickness.

Figure 5d compares the experimentally measured J_{sc} values to predicted J_{sc} values as a function of C_{60} thickness. In Figure 5d, we assume a SWCNT layer thickness of 13 nm, in line with the average thickness of the experimentally studied films, and a C_{60} L_D of 15 nm. The three solid traces display the predicted J_{sc} for three different SWCNT L_D values: 5 nm, 15 nm, and 25 nm. The experimental data all fall within the bounds set by this range of L_D values, with most values falling between $L_D = 5$ nm and $L_D = 15$ nm. These L_D values compare well with recent estimates of the singlet exciton diffusion length within C_{60} ^[32-36] and s-SWCNT films,^[13, 25] lending credence to our optical model. For the 25 nm SWCNT L_D case, the individual contributions of the SWCNT and C_{60} layers are broken out as the dashed and dash-dotted traces, respectively. These traces afford a convenient visualization of how the relative contributions of s-SWCNTs and fullerenes can be finely tuned through optical interferences within the device stack, and provide a robust route for predictive tuning of SWCNT PV solar capture. As summarized in Table 2, the relative contributions of the SWCNTs and C_{60} predicted by our model align well with the values determined experimentally.

Discussion

Although still in the early stages of development, thin films of highly enriched s-SWCNTs hold promise for a number of different opto-electronic devices, including photovoltaics, detectors, field-effect transistors, and photonic elements. Progress towards reliable high efficiency devices benefits from the development of fabrication methodologies that are scalable, reproducible, and produce smooth, uniform films. The ultrasonic spraying process developed here results in highly uniform PFO-wrapped s-SWCNT thin films with very low surface roughness, enabling bilayer PV devices with very thin C_{60} layers. The device with ~ 30 nm C_{60} layer thickness utilizes the thinnest C_{60} layer reported for a s-SWCNT/fullerene bilayer solar cell. In previous device studies, the SWCNT layer has been deposited by iterative doctor-blading,^[3] spin-coating^[14] and vacuum filtration.^[15] Typically, spin-coating and vacuum filtration produce SWCNT films with significant roughness, necessitating thick C_{60} layers to avoid shunting and short-circuited bilayer PV devices.^[14, 15] These thick C_{60} layers may be

problematic for several reasons in bilayer devices. First, as demonstrated here and in previous studies,^[32-36] the singlet exciton diffusion length within C₆₀ films is relatively short (e.g. 7 - 19 nm). Thus, C₆₀ layers significantly thicker than ~20 nm incorporate appreciable material in excess of what is needed to generate photocurrent from that layer. Second, the electron mobility is relatively low in C₆₀, so thicker layers may increase device series resistance. Finally, the reduced visible transmittance of thick C₆₀ layers precludes the devices from being exploited in niche applications, such as semi-transparent solar cells for BIPV. While doctor-bladed films tend to be quite smooth and produce devices with good fill factors,^[3] it isn't clear that this deposition strategy would be scalable for high throughput fabrication of thin SWCNT films (i.e. tens of nanometers) with thicknesses that could be controlled with high precision (i.e. +/- a few nanometers). While techniques such as doctor blading, slot dye, and Gravure coating are generally scalable, they are typically preferred for thin-film applications requiring high-viscosity inks and film thicknesses ranging from hundreds of nanometers to microns.^[29]

As shown here, the (7,5) s-SWCNT/C₆₀ bilayer solar cell provides a useful model system for testing a multiphase optical model that can successfully reconstruct EQE spectra by incorporating the complex index of refraction for each layer within the device. The optical model produces several insights for thin-film SWCNT devices that may aid in predictive fabrication strategies of future devices. The successful reproduction of EQE spectra relies upon the incorporation of singlet exciton diffusion lengths of ~15 nm within each layer. The model also suggests device geometries that optimize J_{SC} in particular regions of the solar spectrum, informing optimization strategies for particular devices. For example, the model suggests that near-infrared photodetectors require C₆₀ thicknesses in the range of ~80 – 90 nm. In contrast, PV devices are optimized at significantly thinner C₆₀ layers (~30 nm), which maximize the photon density absorbed in the visible range of the solar spectrum. Further spectroscopic ellipsometry measurements of s-SWCNT thin films enriched in other chiralities will aid in the application of this model to a plethora of SWCNT devices with tunable solar capture.

The strong performance of our devices with ~32 nm C₆₀ indicates that our ultrasonic spray method of depositing the s-SWCNT absorber layer produces the smooth and uniform films that are necessary to enable ultra-thin devices. Interestingly, the fabrication of bilayer s-SWCNT/C₆₀ devices with ultra-thin (e.g. 20 – 40 nm) acceptor layers opens up the possibility for semi-transparent solar cells. For example, not including the back silver electrode for the device produced with 30 nm of C₆₀, the entire device thickness would only be ~100 nm (which includes the PEDOT and BCP layers). If a transparent low work function electrode, such as an n-type graphene^[37] or SWCNT^[38] thin film, were used in place of silver, the visible transmittance of this device would be in the range of ~70%. Such devices could serve as building-integrated photovoltaic windows, reducing infrared transmittance (low emissivity) and providing power while still allowing significant visible transmittance.

Conclusion

In summary, we have developed a scalable method for spray-coating polyfluorene-wrapped s-SWCNTs that produces films with prescribed thicknesses that are smooth and uniform enough to make strongly rectifying, high-performance devices with a C₆₀ layer as thin as 30 nm, difficult metrics to meet with other SWCNT thin-film deposition techniques. The ultrasonic spraying technique developed here, which is optimized for low-viscosity highly pure s-SWCNT inks in organic solvents, could enable advances not only in SWCNT solar cells, but also in other emerging technologies such as vertical field effect transistors^[39, 40] and light-emitting diodes incorporating s-SWCNT injection layers.^[41, 42] Furthermore, we have refined an optical model for our devices that accurately predicts the current density and relative contributions of the C₆₀ and SWCNT layers to the external quantum efficiency. Combining our optical model and high-precision spray deposition technique, we have the potential to tune the active layer thickness to optimize current extraction for a wide array of device geometries, all within a highly scalable deposition process. Such control enables strategies for the rational optimization of SWCNT:C₆₀ bilayer heterojunctions for an assortment of applications including, PV, BIPV, and photodetectors.

Acknowledgements

This work was funded by the NREL's Laboratory Directed Research and Development (LDRD) program.

$t_{C_{60}}$ (nm)	t_{SWCNT} (nm)	J_{sc} (mA/cm ²)	V_{oc} (V)	FF (%)	PCE (%)
32	14.5	3.93	0.38	54	0.81
53	14.5	3.61	0.41	55	0.82
73	13.0	2.69	0.38	52	0.54
78	10.0	2.35	0.44	59	0.61

Table 1. Device parameter for the four devices shown in Figure 5a/b

$t_{C_{60}}$ (nm)	t_{SWCNT} (nm)	J_{sc} SWCNT (%) Expt.	J_{sc} C ₆₀ (%) Expt.	J_{sc} SWCNT (%) Model	J_{sc} C ₆₀ (%) Model
32	14.5	25	75	26	74
53	14.5	37	63	37	63
73	13.0	46	54	43	57
78	10.0	36	64	43	57

Table 2. Experimental and predicted contributions of SWCNT and C₆₀ layers to J_{sc} for devices in Figure 5a/b

References

- [1] F. Schoppler, C. Mann, T. C. Hain, F. M. Neubauer, G. Privitera, F. Bonaccorso, D. Chu, A. C. Ferrari and T. Hertel, *J. Phys. Chem. C* **2011**, 115, 14682-14686.
- [2] T. Duerkop, S. A. Getty, E. Cobas and M. S. Fuhrer, *Nano Lett.* **2004**, 4, 35-39.
- [3] M. J. Shea and M. S. Arnold, *Appl. Phys. Lett.* **2013**, 102, 243101/243101-243101/243105.
- [4] M. S. Arnold, J. L. Blackburn, J. J. Crochet, S. K. Doorn, J. G. Duque, A. Mohite and H. Telg, *Phys. Chem. Chem. Phys.* **2013**, 15, 14896-14918.
- [5] S. M. Bachilo, M. S. Strano, C. Kittrell, R. H. Hauge, R. E. Smalley and R. B. Weisman, *Science* **2002**, 298, 2361-2366.
- [6] D. D. Tune and J. G. Shapter, *Energy Environ. Sci.* **2013**, 6, 2572-2577.
- [7] D. J. Bindl, A. J. Ferguson, M.-Y. Wu, N. Kopidakis, J. L. Blackburn and M. S. Arnold, *J. Phys. Chem. Lett.* **2013**, 4, 3550-3559.
- [8] D. J. Bindl, M.-Y. Wu, F. C. Prehn and M. S. Arnold, *Nano Lett.* **2011**, 11, 455-460.
- [9] A. J. Ferguson, J. L. Blackburn, J. M. Holt, N. Kopidakis, R. C. Tenent, T. M. Barnes, M. J. Heben and G. Rumbles, *J. Phys. Chem. Lett.* **2010**, 1, 2406-2411.
- [10] J. M. Holt, A. J. Ferguson, N. Kopidakis, B. A. Larsen, J. Bult, G. Rumbles and J. L. Blackburn, *Nano Lett.* **2010**, 10, 4627-4633.
- [11] M. Gong, T. A. Shastry, Y. Xie, M. Bernardi, D. Jasion, K. A. Luck, T. J. Marks, J. C. Grossman, S. Ren and M. C. Hersam, *Nano Lett.* **2014**.
- [12] Y. Ye, D. J. Bindl, R. M. Jacobberger, M.-Y. Wu, S. S. Roy and M. S. Arnold, *Small* **2014**, 3299-3306.
- [13] D. J. Bindl and M. S. Arnold, *J. Phys. Chem. C* **2013**, 117, 2390-2395.
- [14] M. P. Ramuz, M. Vosgueritchian, P. Wei, C. Wang, Y. Gao, Y. Wu, Y. Chen and Z. Bao, *ACS Nano* **2012**, 6, 10384-10395.
- [15] R. M. Jain, R. Howden, K. Tvrdy, S. Shimizu, A. J. Hilmer, T. P. McNicholas, K. K. Gleason and M. S. Strano, *Adv. Mater.* **2012**, 24, 4436-4439.
- [16] A. Nish, J.-Y. Hwang, J. Doig and R. J. Nicholas, *Nat Nano* **2007**, 2, 640-646.
- [17] T. M. Barnes, J. D. Bergeson, R. C. Tenent, B. A. Larsen, G. Teeter, K. M. Jones, J. L. Blackburn and J. van de Lagemaat, *Appl. Phys. Lett.* **2010**, 96, -.

- [18] T. M. Barnes, M. O. Reese, J. D. Bergeson, B. A. Larsen, J. L. Blackburn, M. C. Beard, J. Bult and J. van de Lagemaat, *Adv. Energy Mater.* **2012**, 2, 353-360.
- [19] R. C. Tenent, T. M. Barnes, J. D. Bergeson, A. J. Ferguson, B. To, L. M. Gedvilas, M. J. Heben and J. L. Blackburn, *Adv. Mater. (Weinheim, Ger.)* **2009**, 21, 3210-3216.
- [20] A. F. Hebard, R. C. Haddon, R. M. Fleming and A. R. Kortan, *Appl. Phys. Lett.* **1991**, 59, 2109-2111.
- [21] L. A. A. Pettersson, L. S. Roman and O. Inganäs, *J. Appl. Phys.* **1999**, 86, 487-496.
- [22] L. A. A. Pettersson, L. S. Roman and O. Inganäs, *J. Appl. Phys.* **2001**, 89, 5564-5569.
- [23] M. Law, M. C. Beard, S. Choi, J. M. Luther, M. C. Hanna and A. J. Nozik, *Nano Lett.* **2008**, 8, 3904-3910.
- [24] M.-Y. Wu, R. M. Jacobberger and M. S. Arnold, *J. Appl. Phys. (Melville, NY, U. S.)* **2013**, 113, 204504/204501-204504/204515.
- [25] D. J. Bindl, M. J. Shea and M. S. Arnold, *Chem. Phys.* **2013**, 413, 29-34.
- [26] J. L. Blackburn, J. M. Holt, V. M. Irurzun, D. E. Resasco and G. Rumbles, *Nano Lett.* **2012**, 12, 1398-1403.
- [27] K. S. Mistry, B. A. Larsen and J. L. Blackburn, *ACS Nano* **2013**, 7, 2231-2239.
- [28] S. H. Chen, A. C. Su and S. A. Chen, *J. Phys. Chem. B* **2005**, 109, 10067-10072.
- [29] F. C. Krebs, *Sol. Energy Mater. Sol. Cells* **2009**, 93, 394-412.
- [30] A. D. Willey, J. M. Holt, B. A. Larsen, J. L. Blackburn, S. Liddiard, J. Abbott, M. Coffin, R. R. Vanfleet and R. C. Davis, *Journal of Vacuum Science & Technology B* **2014**, 32, 011218.
- [31] Y. Battie, D. Jamon, A. En Naciri, J.-S. Lauret and A. Loiseau, *Appl. Phys. Lett.* **2013**, 102, -.
- [32] J. J. M. Halls, K. Pichler, R. H. Friend, S. C. Moratti and A. B. Holmes, *Appl. Phys. Lett.* **1996**, 68, 3120-3122.
- [33] M. C. Fravventura, J. Hwang, J. W. A. Suijkerbuijk, P. Erk, L. D. A. Siebbeles and T. J. Savenije, *J. Phys. Chem. Lett.* **2012**, 3, 2367-2373.
- [34] L. A. A. Pettersson, L. S. Roman and O. Inganäs, *J. Appl. Phys.* **1999**, 86, 487-496.
- [35] P. A. Lane, P. D. Cunningham, J. S. Melinger, G. P. Kushto, O. Esenturk and E. J. Heilweil, *Phys. Rev. Lett.* **2012**, 108, 077402.

- [36] F. Monestier, J.-J. Simon, P. Torchio, L. Escoubas, B. Ratier, W. Hojeij, B. Lucas, A. Moliton, M. Cathelinaud, C. Defranoux and F. Flory, *Appl. Opt.* **2008**, 47, C251-C256.
- [37] J. B. Bult, R. Crisp, C. L. Perkins and J. L. Blackburn, *ACS Nano* **2013**, 7, 7251-7261.
- [38] K. S. Mistry, B. A. Larsen, J. D. Bergeson, T. M. Barnes, G. Teeter, C. Engtrakul and J. L. Blackburn, *ACS Nano* **2011**, 5, 3714-3723.
- [39] B. Liu, M. A. McCarthy, Y. Yoon, D. Y. Kim, Z. Wu, F. So, P. H. Holloway, J. R. Reynolds, J. Guo and A. G. Rinzler, *Adv. Mater.* **2008**, 20, 3605-3609.
- [40] B. Liu, M. A. McCarthy and A. G. Rinzler, *Adv. Funct. Mater.* **2010**, 20, 3440-3445.
- [41] W. Xu, J. Zhao, L. Qian, X. Han, L. Wu, W. Wu, M. Song, L. Zhou, W. Su, C. Wang, S. Nie and Z. Cui, *Nanoscale* **2014**, 6, 1589-1595.
- [42] M. C. Gwinner, F. Jakubka, F. Gannott, H. Sirringhaus and J. Zaumseil, *ACS Nano* **2011**, 6, 539-548.